Published in final edited form as:
J Magn Reson. 2010 July ; 205(1): 1–8. doi:10.1016/j.jmr.2010.02.020.

DUAL FREQUENCY RESONATOR FOR 1.2 GHZ EPR/16.2 MHZ NMR CO-IMAGING

Sergey Petryakov, **Alexandre Samouilov**, **Eric Kesselring**, **George L. Caia**, **Ziqi Sun**, and **Jay L. Zweier***
Center for Biomedical EPR Spectroscopy and Imaging, the Davis Heart and Lung Research Institute, and the Division of Cardiovascular Medicine, the Department of Internal Medicine, The Ohio State University College of Medicine, Columbus, Ohio 43210

Abstract

The development of a dual frequency resonator that enables both EPR and proton NMR imaging within the same resonator, magnet and gradient system is described. A novel design allows the same resonator to perform both EPR and proton NMR operation without moving resonator cables or switches. The resonator is capable of working at frequencies of 16.18 MHz for proton NMR and 1.2 GHz for EPR and is optimized for isolated rat heart experiments, measuring 22 mm in inner diameter and 19 mm in length. In EPR mode, the resonator functions as a one loop two gap resonator, electrically coupled through a half wavelength inverter. In NMR mode, it functions a single turn coil. Using the same loop for both modalities maximizes filling factor at both frequencies. Placing the tuning and switching controls away from the resonator prevents any inadvertent movement that would cause errors of EPR and NMR co-imaging registration. The resonator enabled good quality EPR and proton MRI of isolated rat hearts with precise registration.

INTRODUCTION

EPR imaging (EPRI) can be applied to obtain the spatial distribution of free radicals and their spectral characteristics in samples by utilizing magnetic field gradients, in a manner similar to that of MRI. Therefore spatial EPRI and spectral-spatial EPRI are valuable tools in biology for *in vivo* study and visualization of functional properties including tissue oxygenation, acidity and redox status [1–5]. The EPR images obtained contain information about the spatial location of the free radical probe but often lack the anatomic structure required for interpretation. In contrast, proton MRI (PMRI) is an ideal approach to provide anatomic information through EPRI and PMRI image registration. While this can be performed using separate EPRI and PMRI instrumentation [6–10]; the use of separate instruments requires time consuming registration of the two coordinate frames, and the movement of the animal or sample from EPR to NMR system limits the quality of this image registration and greatly restricts or prevents the performance and real time evaluation required for many experimental protocols.

*Address for correspondence and proofs: Jay L. Zweier, Davis Heart and Lung Research Institute, 473 West 12th Avenue, Room 110G, Columbus, OH 43210-1252. jay.zweier@osumc.edu.

The concept of a hybrid system with common magnet and field gradients for EPR/NMR co-imaging has been described [11–16]. We have previously reported the development of a coimaging system that utilizes a large iron core electromagnet and is capable of performing fast transition from low field EPR measurements to proton MRI measurements at much higher fields [11,17]. A common EPRI/MRI gradient set is utilized to assure a common image coordinate system with automatic registration of the EPR and proton MR images. In order to eliminate movement of the sample relative to the magnetic field gradient coordinate system, a dual-purpose resonator assembly was developed containing EPR and proton NMR resonators with a stage that enables each resonator to slide precisely into place around a fixed sample holder located at the center of the gradient system. The architecture of the stage was chosen to facilitate in vivo animal experiments by loading the animal either through the top of the sample holder or from the front side of the magnet through the support tubes. This method allows using separate optimized EPR and proton NMR resonators. However, this approach while workable and useful, has a number of practical problems or inconveniences especially for experiments with smaller objects like perfused rat hearts. These include:

- **i.** The overall length of the sliding resonator stage is triple that of the resonator, which makes the assembly bulky and initial precise positioning of the resonator stage difficult.
- **ii.** The resonator stage blocks access and reduces the visibility of the sample after the setup is placed in the magnet.
- **iii.** Resonators can not be tuned prior to the experiment; tuning can be done only during change of the acquisition modality. So it takes additional time to re-tune and re-couple the resonators each time they are switched.
- **iv.** Movement of the resonators can inadvertently induce movements of the overall stage and sample.

These problems can be limited individually by modifying the resonators and resonator stage. Of note, a configuration positioning the EPR resonator inside a larger solenoidal coil NMR resonator tuned at different frequencies has been previously reported but produces detrimental effects on the performance of the NMR resonator [13–15]. In view of these issues, a single resonator design capable of accommodating both modalities with dual resonant frequencies would be desirable since it would completely eliminate all these problems, providing a simpler more space efficient approach for coimaging, saving critical time in experimental applications, allowing more precise EPR/NMR coimaging.

Dual frequency resonators for NMR applications have been extensively described that were designed for $^{1}H/^{19}F$, $^{1}H/^{13}C$, or similar experiments [18–20]. In these pure fixed field NMR applications the resonance frequencies for the nuclei studied are typically relatively close differing by ≤ 3 fold. For our EPR/NMR coimaging system and applications, the ratio between frequencies is much larger ~ 74 considering L-band EPR at ~1200 MHz and 16.2 MHz proton MRI [11]. Also quality factor requirements for EPR spectroscopy and imaging are quite different from that of proton MRI.

Surface coil resonators currently available for use in L-band (typically around 1.2 GHz) are limited to useful apertures of less than 10 mm limiting the practical use of these resonators to isolated heart and small animal in-vivo applications [21,22]. This diameter is limited by frequency to about one quarter wave length in the conductor. To accommodate larger samples a multigap design is required. For 1.2 GHz L-band frequencies, single loop multiple gap designs afford a larger sample size, improve B_1 field homogeneity and minimize dielectric losses compared to a single gap design as it reduces the electric field in the sample

area [17,23–25]. In contrast, for proton NMR operation at 16.2 MHz, a single gap resonator provides adequate efficiency and minimal dielectric losses.

In this report, we describe a novel resonator design capable of working at 16.2 MHz for proton MRI and 1.2 GHz for EPRI with size suitable for studies of the isolated rat heart. In EPR mode, the resonator functions as a one loop two gap resonator, electrically coupled through a half wavelength inverter, while in NMR mode, it functions as a single turn coil. Using the same loop for both modalities maximizes filling factor at both frequencies and facilitates precise EPR/NMR coimaging by removing the need for any sample or resonator movement.

RESONATOR DESIGN

The EPR section of the dual frequency resonator is constructed as a one loop two gap resonator (Figure 1). The structure of the resonator contains an inductive loop and two pairs of capacitive elements (**A**), with dimensions of these elements forming a λ/2 symmetric resonator. To satisfy this requirement, the length of the capacitive elements is 19 mm on each side, 19 mm wide with a 22 mm loop diameter for the desired 1.2 GHz (Figure 1). Initial estimate for frequency dependent dimensions of the resonator loop was performed according to [26–28]. The capacitive elements had a gap of 2.3 mm

Capacitive coupling for 1.2 GHz is performed through a 50 Ohm 1 mm diameter coaxial cable (**G**) forming a λ/2 EPR inverter connected to the end of the capacitive element (**A**) of the resonator using a 0.2 pF capacitor (**L**). Coupling adjustment is performed by variable capacitive divider (C1, C2). Each half of the capacitive element has an EPR frequency tuned quarter wavelength ($\lambda^{EPR}/4$) transmission line (**B**) connected to both sides. One $\lambda^{EPR}/4$ transmission line end pair couples to an 800 pF capacitor (**K**) and the electrically coupled NMR feed to form the NMR end. The opposite, EPR end of the λ/4 EPR transmission line pair is physically shorted with a specially attached contact forming an L-band tuned balun at the EPR end (**I)** on Figure 1A. At EPR frequencies, the transmission lines connected to the 800 pF capacitor appear as high impedance (*Z*) to the EPR resonator electrodes, minimizing any undesired NMR resonator effects. The higher impedance lines are desirable to maximize resonator filling factor since the λ/4 transmission lines behave like a resonator and trap a portion of the total energy inside the resonator. This results in an apparent decrease of filling factor. The distribution of the currents between the resonator and transmission lines is proportional to $1/Z_{in}$ of the λ/4 transmission line and *Z* of the resonator [29, 30].

In order to minimize any decrease in filling factor, the area of the transmission lines (**B**) was reduced by narrowing the width of transmission line electrodes from 19 to 7 mm, thus increasing the impedance of the transmission line by a 19/7 factor. We did not take into account transmission line distributed inductance due to its small contribution compared to the inductance of the loop. The λ/4 7 mm wide transmission line connecting the electrode and connection plate at the EPR end has higher impedance since the distribution capacitance is 19/7 times smaller. This allowed reducing transmission line induced deterioration of filling factor from ~50 % to ~21 %. Further decrease of transmission-line width was problematic due to negative effect on the performance of the resonator at NMR frequencies. The final efficiency loss depends on the loading capability of the resonator. This loss is a compromise required for dual mode operation and electrical coupling. These considerations are for empty resonators. Loaded resonators exhibit different power distribution characteristics, especially when impedance and Q factor changes with load. The influence of load on impedance and resonance frequency was not taken into consideration, since calculations of loaded resonators are complicated by the uncertain characteristics of living samples. Transmission line loss becomes a smaller proportion of the total as dielectric losses

within the sample load increase. Since a loaded resonator typically has a lower resonant frequency, the length of the λ/4 transmission lines should be slightly longer. For best performance, resonator dimensions can be optimized for a particular sample and load. In our case, final dimensions were experimentally adjusted for isolated rat heart experiments at 1.2 GHz.

During 16.2 MHz NMR operation, the balun on the EPR end functions as a short for the single gap NMR resonator. The 0.2 pF coupling capacitors (**L**) on the EPR end appear as high impedance with minimal effect.

Ideally, an optimally matched resonator should have reactance that matches the preamplifier, thus eliminating the matching circuit. Our one loop design has low impedance and requires a circuit to match the input reactance of the preamplifier. A traditional commercial Resonex NMR tuning and matching circuit is connected to the 800 pF gap of the resonator through a symmetric 100 Ohm impedance ribbon cable. At the low PMRI working frequency of 16.2 MHz, the additional loss in the matching circuit will be small in comparison with the loss in the resonator.

RESONATOR CONSTRUCTION

The general concept of this resonator is schematically shown in Figure 1. The resonator body is constructed from two halves (**D**) of 166 mm × 67 mm × 25.4 mm thick low dielectric loss #1422 Rexolite polystyrene fastened together. Each 25.4 mm thick half has a 19 mm wide slot for the capacitive elements, transmission lines and one half of a 22 mm cylindrical bore (**H**) for the sample. A 67 mm outer dimension ensures the distance between the outer shielding and resonator elements are separated by at least twice the diameter of the loop to improve B_1 homogeneity [31]. A 0.5 μm silver coating is sputtered on the outer surfaces of the Rexolite body for RF shielding. This small silver thickness is adequate for RF shielding at L-band EPR frequencies and allows NMR gradient and modulation coil frequencies to pass without distortion.

The capacitive elements (**A**) and transmission lines (**B**) are formed from 11 μm thick silver strips. These transmission line elements simultaneously serve as capacitors for the low frequency NMR resonator. Total length of the higher frequency EPR portion of the resonator including loop is 60 mm. The 2.3 mm gap separating capacitor and transmission line elements in the Rexolite body halves of the resonator is formed by two opposing 1.15 mm slots (**F**) machined in the body halves (**D**). Transmission lines designed for quarter wavelength of the EPR frequency are made as extension of the capacitor plates and measure 44 mm long, 7 mm wide on the EPR side and 46 mm long and 7 mm wide on the NMR side. The extra 2 mm is needed since the 800 pF capacitor requires the transmission line to be slightly longer than necessary for an ideal short to provide higher impedance and isolation during EPR operation [32]. Rectangular 8 mm × 19 mm connection plates (**C**) are formed at the four ends of the tranmission line elements for connecting the coupling circuit. These plates are located beyond the 800 pF capacitor on the NMR side and beyond the shorting point on the EPR side so they are not included in the resonator circuit. The EPR feeding line consists of a 57 mm piece of semi-rigid 1 mm diameter coaxial cable (**G**). The outer shield contacts the full length of the top 7 mm wide transmission line extension plate (**C**) and only the outer end portion of the bottom 7 mm transmission line extension plate (**B**). The center conductor of this 57 mm semi-rigid line connects to the bottom capacitor element through a 0.2 pF capacitor made from Rogers high frequency laminated plastic sheet. In general, it is similar to the surface coil resonator feeding line designed by Hirata and colleagues [33]. The semi-rigid coax outer shield functions as a continuous connection to the one tranmission line element and point connector to the end of the opposite electrode on the EPR side.

Another important requirement for the combined NMR/EPR resonator is the presence of modulation coils suitable for CW EPR operation. These must also be "transparent" to the pulsed NMR field gradients. Our experimental tests have shown that even very small metal objects near the NMR resonator cause distortions and degrade image quality due to the formation of eddy currents. To minimize this distortion, Helmholtz type modulation coils were constructed with a single layer of 2 mm Litz wire, consisting of multiple 30 μm diameter conductors (New England Electric Wire Corporation, Lisbon NH, NELD1050/46SNSN). Each 128 mm average diameter coil (**M** on Fig. 1B) was attached in the center of 6 mm × 190 mm × 170 mm polystyrene panel (**O**) and positioned 64 mm apart using spacers (**N**). Experimental tests demonstrated no NMR image degradation with disconnected EPR modulation coils.

EQUIVALENT LUMPED ELEMENT CIRCUIT RESONATOR

Addition of transmission lines to both sides of the EPR resonator may cause loss of filling factor and degradation of the quality factor, *Q*. In order to evaluate this, we analyzed an equivalent lumped element circuit, as shown in Fig. 2C. All capacitances in the resonator are calculated as simple parallel plate capacitors. Inductance for the 22 mm diameter loops are calculated according to [34]. The characteristic impedance of the transmission lines (Z_t) is determined by resonator dimensions and is calculated using [35] producing Z_t = 33 Ω. L_t values were obtained using its relationship with $Z_t = \sqrt{L_t/C_t}$. Parameters of calculations are presented below:.

L_r= 0.045 μH inductance of the half 22 mm in diameter loop;

C_g= 1.56 pF capacitance formed by the 19 mm width EPR resonator capacitive elements;

R_g = 0.0197 Ω resistance of the main loop conductor;

L_t = 0.0014 μH equivalent distributed inductance of the 7 mm wide transmission lines;

C_{t1} = 1.34 pF equivalent distributed capacitance of the 7 mm wide, 44 mm long transmission lines;

C_{t2} = 1.4 pF equivalent distributed capacitance of the 7 mm wide, 46 mm long transmission lines;

R_t = 0.0535 Ω equivalent distributed resistance of the 7 mm wide transmission lines.

We considered the resistive loss in conductor only for an empty resonator. The contribution of the dielectric loss of the Rexolite is considered negligible in the calculations since it is much smaller than electrode conductive losses. Losses in the strip conductors for L-band frequency are inversely proportional to the width of the conductive strip. Assuming equal element length of EPR resonator and transmission lines, the ratio of resistive losses in transmission lines and resonator is 19/7 when considering the main λ/2 symmetric resonator 19 mm wide strip electrodes and two λ/4 7 mm wide transmission lines.

The measured Q of the entire resonator including all transmission lines and matching elements, Q_{res}, is approximately 195, which consists of

$$1/Q_r = 1/Q_{gap} + 1/Q_{\text{transmission line}}$$
$$Q = \omega L_{gap}/R_{gap}. \quad R_{gap} = 0.0197\,\Omega,$$
$$R_{\text{transmission line}} = R_{gap} \bullet 19/7 = 0.0534\,\Omega$$
$$Q_{gap} = 17200,\ Q_t = 220,\ Q_r \gg Q_t,$$

where the Q_{gap} number is large since it assumes an ideal resonator (completely shielded without radiation losses). Practically, the maximum Q of the empty resonator is limited by the Q of the transmission lines. Lossy samples reduce the Q of the main resonator, not the Q of the transmission lines. Since we are working with relatively lossy samples, the reduction in Q from the transmission lines is a small proportion of the total loss. C1 and C2 – equivalent capacitive divider of the coupling circuit, C1 = 0.2 pF, C2 = 1 to 8 pF (see figure 2C). For the NMR resonator, the sum of inductances is 0.0928 μ H and the sum of parallel capacitances is 928 pF.

TESTING AND EXPERIMENTAL RESULTS

We measured the absolute intensity of the B_1 with a 4.0 mm diameter brass sphere using the perturbing spheres method [36,37]. The measurement of B_1 distribution was performed in the resonator loaded with 18 mm diameter 18 mm long cylinder filled with 0.5 mm glass spheres. Voids between glass spheres were filled with saline solution. This phantom simulates tissue load and allowed free positioning of the brass sphere. The brass sphere was cemented to a quartz rod and its position was controlled by a micro-positioning device. For comparison, a reentrant resonator with 25 mm sample loop diameter similar to the design described in [38] was used. Frequency shift was monitored using an Agilent 8719ES vector network analyzer at 3.2 mW power. The B_1 field of the Dual Frequency Resonator was $0.011\,\text{mT}/\sqrt{W}$, with a Q of 195, while the B_1 value of the loaded resonator $G/\sqrt{W}$ (Glass beads + 3.5 cc 14% saline was 0.008 mT with a Q of 97.5). For the reentrant resonator the B_1 field was $0.010\,\text{mT}/\sqrt{W}$, unloaded Q=301, while the $B_1/\sqrt{W}$ of the loaded resonator (Glass beads + 3.5 cc 14% saline was $0.007\,\text{mT}/\sqrt{W}$ with a Q of 97) was $B_1 = 0.006\,\text{mT}/\sqrt{W}$ (Glass beads + 3.5 cc 14% saline). As seen from Table 1, the reentrant resonator slightly outperforms the dual frequency resonator at loads smaller than 2.5 cc. However, at larger loads, the dual frequency resonator performance is similar to the reentrant resonator.

Resolution and accuracy of co-registration was evaluated by acquiring the image of a specially constructed phantom of tubes of different sizes filled with 1 mM tetrathiatriarylmethyl radical, CT-03 (TAM) [39,40] (Figure 3). The phantom consisted of 20 mm long clusters of capillary tubes of 1.3 mm ID (A), 0.9 mm ID (B), 0.5 mm ID (C), 2 tubes of 6 mm ID with TAM surrounding voids from packed 0.4 mm OD rods (D), 1 tube of 6 mm ID with TAM surrounding voids from packed 0.3 mm OD rods (E). The central 3 large tubes were arranged into a triangular shaped pattern, and all were packed into an 18 mm i.d. plastic cylinder. Images of this phantom demonstrated good sensitivity and accurate coregistration for EPR and NMR modes (Figure 3).

B_1 field homogeneity is a critical characteristic of resonator performance for imaging applications. A specially constructed phantom similar to the geometry of the isolated rat heart was imaged to further evaluate resonator performance and B_1 field homogeneity. The phantom was a 18 mm inner diameter 18 mm height cylinder with conical insert (Figure 4). The cylinder was filled with an aqueous 1.0 mM solution of TAM in 30% normal saline 4 cc volume This type of phantom loads the resonator similar to an isolated rat heart. The whole phantom was visible in both modes showing sufficient active volume for the isolated rat

heart experiment. The near uniform intensity of the images confirms good B_1 homogeneity of the resonator along all axes in both modes.

In order to evaluate the applicability of the resonator for biological applications, images of isolated rat hearts infused with 1 mM TAM were performed (Figure 5). The hearts were from male rats of about 350 g weight supplied from Charles River Laboratories (Wilmington, MA). Imaging was performed on the EPR/NMR co-imaging system described previously but the new dual resonator was used in place of the prior sliding resonator assembly [11]. The dual resonator was positioned coaxially in the center of the gradients in order to exclude the need for the moving stage as required in the earlier setup. The loaded resonator was tuned for both frequencies prior to acquisition. The aortic cannula is identified at the top of the vertical slices. The LV cavity is clearly seen as the central void and the two imprints from plastic support tubes used to center heart in the resonator appear on the 3D rendering. Good stability was observed in these studies enabling continued imaging for periods of up to 3 hours. The present resonator coupling capabilities are limited by the single gap electrical coupling design. Coupling capability could be improved two times with an additional coupling feed. Also, the resonator diameter is limited to one quarter wave length in the conductor, which is about 22 mm for the two gap LG resonator at 1.2 GHz. Thus, the size and coupling was well suited for typical experiments in the isolated rat heart model.

DISCUSSION

While EPR imaging is a powerful technique capable of mapping the location of free radicals in a variety of samples, for biomedical applications proton MRI coimaging is very helpful providing critical and precise anatomic registration that is needed for interpretation of organ specific free radical localization. In this report, we have presented a novel dual mode EPR/NMR resonator design that allows the same resonator to perform both EPR and proton NMR operation without moving resonator cables or switches. The resonator was designed to enable EPR/NMR coimaging for isolated rat heart experiments. In EPR mode, the resonator functions at 1.2 GHz as a one-loop two-gap resonator, electrically coupled through a half wavelength inverter. In NMR mode at 16.2 MHz, it functions as a single turn coil. Using the same loop for two modalities maximizes filling factor at both frequencies and prevents any inadvertent movement that would cause errors of EPR and NMR co-imaging registration.

For broad band NMR applications a variety of dual frequency resonators have been previously described that enable measurements of different nuclei such as $^{1}H/^{19}F$, $^{1}H/^{13}C$, or others [18–20]. In these pure fixed field NMR applications the resonance frequencies for the nuclei studied are typically relatively close differing by ≤ 3 fold so that simple adjustment or change of the tuning capacitor can be used to achieve the second resonant frequency. A prio double resonator design for EPRI and NMRI has been described in by Alfonsetti et al. [14]. This design is for pulsed experiments with a frequency ratio of 660, with both EPR and NMR performed at the same magnetic field. The described “composite resonator” consists of a coaxial combination of a one-loop-two gap EPR resonator and solenoidal coil NMR resonators. This setup has separate EPR and NMR parts. The drawback of this approach is significant deterioration of NMR performance due to lowering of the filling factor, which is caused by the increased diameter due to the EPR section inside the NMR section. The closeness of the EPR section to the NMR section also lowers the NMR section Q. More importantly, conductive sections from the EPR resonator are in the close proximity to the sample inside the NMR coil and generate eddy currents induced by fast switching MRI gradients, causing severe distortion of the NMR image [15]. We chose a different approach by using the same loop for EPRI and MRI which is free from the above weaknesses, giving the same filling factor for both modalities.

For our EPR/NMR coimaging applications, the ratio between frequencies is ~ 74 considering L-band EPR at ~1200 MHz and 16.2 MHz proton MRI [11]. Our design once appropriately tuned and coupled inherently enables both EPR and NMR operation without any further adjustments. A prior report first demonstrated the concept of a dual frequency transmission line/loop-gap resonator for CW EPR/CW MRI imaging with EPR at 680 MHz and NMR at 27.7 MHz has been previously reported [32]. There are a number of differences in our design concept and this earlier report. In contrast to our design that utilizes capacitive coupling, this earlier design used a magnetic coupling mechanism for both frequencies that can be vibration-prone and not compatible with standard pulsed MRI due to interaction with the gradient pulses. This design was only utilized for CW proton MRI, and as such was not suitable to produce high quality MRI data in biomedical applications. It also required movement and replacement of the RF source cable and changes in coupling adjustments to transition from EPR to NMR mode, while our design does not.

Our dual resonator design was shown in a series of phantoms and isolated heart experiments to be well suited for high quality EPR imaging and proton MRI enabling dual mode image acquisition with a high degree of accuracy in image registration. The independent EPR and NMR operation with no need for resonator adjustment in shifting modes, facilitated rapid transition from NMR to EPR operation and, along with the common field gradients used, enabled precise image registration. The common resonator loop allowed a high filling factor in both modes with relatively high Q providing good sensitivity for both EPR and proton MRI, comparable to other optimized resonators suitable for this sample size. Although the resonator was tested for PMRI/CW EPRI coimaging applications, we do not see any fundamental limitations for adaptation of this design approach for DNP experiments. However, some redesign to improve heat dissipation will be necessary. Higher power EPR irradiation is required for DNP/PEDRI compared to CW EPR imaging.

CONCLUSION

The dual frequency resonator for EPR/NMR coimaging allows both EPR and proton NMR operation without moving cables or switches on the resonator, reducing sample disturbances and total experiment time. With the same sample volume for NMR and EPR, filling factor can be optimized for both modes. Sensitivity, and image contrast and resolution was comparable to traditional separate EPR and NMR resonators. Effective high quality EPRI and MRI images of isolated hearts were obtained with intrinsic precise co-registration.

Acknowledgments

This work was supported by NIH Research Grants EB0890 and EB4900. We thank Mr. Levy Reyes for support with the isolated heart preparations

References

1. Halpern, HJ. In Vivo EPR (ESR): Theory and Applications. Berliner, LJ., editor. Springer; New York: 2003. p. 117-183.
2. Kuppusamy P, Zweier JL. Cardiac applications of EPR imaging. NMR Biomed 2004;17:226–239. [PubMed: 15366025]
3. Yokoyama H, Lin Y, Itoh O, Ueda Y, Nakajima A, Ogata T, Sato T, Ohya-Nishiguchi H, Kamada H. Free Radic Biol Med 1999;27:442–448. [PubMed: 10468220]
4. Zweier JL, Kuppusamy P. Electron paramagnetic resonance measurements of free radicals in the intact beating heart: a technique for detection and characterization of free radicals in whole biological tissues. Proc Natl Acad Sci USA 1988;85:5703–5707. [PubMed: 2840672]
5. Khramtsov VV, Grigor'ev IA, Foster MA, Lurie DJ. In vitro and in vivo measurement of pH and thiols by EPR-based techniques. Antioxid Redox Signaling 2004;6:667–676.

6. Elas M, Bell R, Hleihel D, Barth ED, McFaul C, Haney CR, Bielanska J, Pustelny K, Ahn KH, Pelizzari CA, Kocherginsky M, Halpern HJ. Electron paramagnetic resonance oxygen image hypoxic fraction plus radiation dose strongly correlates with tumor cure in FSa fibrosarcomas. Int J of Rad Onc, Biol, Phys 2008;71:542–549.
7. Elas M, Williams BB, Parasca A, Mailer C, Pelizzari CA, Lewis MA, River JN, Karczmar GS, Barth ED, Halpern HJ. Quantitative tumor oxymetric images from 4D electron paramagnetic resonance imaging (EPRI): methodology and comparison with blood oxygen level-dependent (BOLD) MRI. Magn Reson Med 2003;49:682–91. [PubMed: 12652539]
8. Krishna MC, English S, Yamada K, Yoo J, Murugesan R, Devasahayam N, Cook JA, Golman K, Ardenkjaer-Larsen JH, Subramanian S, Mitchell JB. Overhauser enhanced magnetic resonance imaging for tumor oximetry: coregistration of tumor anatomy and tissue oxygen concentration. Proc Natl Acad Sci U S A 2002;99:2216–21. [PubMed: 11854518]
9. Hyodo F, Yasukawa K, Yamada K, Utsumi H. Spatially Resolved Time-Course Studies of Free Radical Reactions With an EPRI/MRI Fusion Technique. Magn Reson in Med 2006;56:938–943. [PubMed: 16964613]
10. He G, Deng Y, Li H, Kuppusamy P, Zweier JL. EPR/NMR Co-imaging for Anatomic Registration of Free- Radical Images. Magn Reson Med 2002;47:571–578. [PubMed: 11870845]
11. Samouilov A, Caia GL, Kesselring E, Petryakov S, Wasowicz T, Zweier JL. Development of a hybrid EPR/NMR co-imaging system. Magn Reson Med 2007;58:156–166. [PubMed: 17659621]
12. Kawada Y, Hirata H, Fujii H. Use of multi-coil parallel-gap resonators for co-registration EPR/NMR imaging. J Magn Reson 2007;184:29–38. [PubMed: 17029883]
13. Di Giuseppe S, Placidi G, Sotgiu A. New experimental apparatus for multimodal resonance imaging: initial EPRI and NMRI experimental results. Phys Med Biol 2001;46:1003–1016. [PubMed: 11324947]
14. Alfonsetti M, Del Vecchio C, Di Giuseppe S, Placidi G, Sotgiu A. A composite resonator for simultaneous NMR and EPR imaging experiments. Meas Sci Technol 2001;12:1325–1329.
15. Placidi G, Alecci M, Sotgiu A. First imaging results obtained with a multimodal apparatus combining low-field (35.7 mT) MRI and pulsed EPRI. Phys Med Biol 2002;47:N127–N132. [PubMed: 12069098]
16. Matsumoto S, Nagai M, Yamada K, Hyodo F, Yasukawa K, Muraoka M, Hirata H, Ono M, Utsumi H. A Composite Resonator Assembly Suitable for EPR/NMR Coregistration Imaging. Magn Reson Engin 2005;25 B:1–11.
17. Petryakov S, Samouilov A, Kesselring E, Wasowicz T, Caia GL, Zweier JL. Single loop multi-gap resonator for whole body EPR imaging of mice at 1.2 GHz. J of Magn Reson 2007;188:68–73. [PubMed: 17625940]
18. Wood RL, Froncisz W, Hyde JS. The Loop-Gap Resonator. II. Controlled Return Flux Three-Loop, Two-Gap Microwave Resonators For ENDOR and ESR Spectroscopy. J Magn Reson 1984;58:243–253.
19. Hyde JS, Yin J, Froncisz W, Feix JB. Electron-Electron Double Resonance (ELDOR) with a Loop-Gap resonator. J Magn Reson 1985;63:142–150.
20. Dirksen P, Disselhorst AJM, Meer HV, Wenckebach WT. A Loop-Gap Resonator for Microwave-Induced Optical Nuclear Polarization, Electron Spin-Echo Experiments, and Dynamic Nuclear Polarization. J Magn Reson 1990;87:516–522.
21. Salikhov I, Hirata H, Walczak T, Swartz HM. An improved external loop resonator for in vivo L-band EPR spectroscopy. J Magn Reson 2003;164:54–59. [PubMed: 12932455]
22. Hirata H, Walczak T, Swartz HM. Electronically tunable surface-coil-type resonator for L-band EPR spectroscopy. J Magn Reson 2000;142:159–167. [PubMed: 10617447]
23. Piasecki W, Froncisz W. Field distributions in loop-gap resonators. Meas Sci Technol 1993;4:1363–1369.
24. Ghim BT, Rinard GA, Quine RW, Eaton SS, Eaton GR. Design and Fabrication of Copper-Film Loop–Gap Resonators. J Magn Reson, Series A 1996;120:72–76.
25. Wojciech P, Wojciech F. Field distributions in loop-gap resonators. Meas Sci Technol 1993;4:1363–1369.

26. Hirata H, Ono M. Resonance frequency estimation of a bridged loop-gap resonator used for magnetic resonance measurements. Rev Sci Instrum 1996;67:73–78.
27. Hyde, JS.; Froncisz, W. Loop gap resonators. In: Hoff, AJ., editor. Advanced EPR: Applications in Biology and Biochemistry. Elsevier; Amsterdam: 1989. p. 277-306.
28. Mehdizadeh, A. PhD Thesis. Milwaukee, Wisconsin: Marquette University; 1983. An Investigation on Electromagnetic Fields and Properties of the Loop-Gap Resonator, a Lumped Mode Microwave Resonant Structure.
29. Shirman, YD. Electronic Systems Construction Foundations and Theory Handbook (in Russian). Makvis; Moscow: 1998. p. 250-252.
30. Shipman, AR. Theory and Problems of Transmission Lines. Vol. Chapter 10. McGRAW-HILL BOOK COMPANY; p. 215-223.
31. Eaton, SR.; Eaton, GR.; Berliner, LJ. Biomed. EPR, Part B. In: Williams, BB.; Halpern, HJ., editors. In vivo EPR Imaging. Vol. Chapter 11. Kluwer Academic/Plenum Publishers; 2005. p. 290
32. Sato T, Oikawa K, Ohya-Nishiguchi H, Kamada H. Development of an L-band electron spin resonance/proton nuclear magnetic resonance. Rev Sci Instrum 1997;68:2076–2081.
33. Hirata H, He G, Deng Y, Salikhov I, Petryakov S, Zweier JL. A loop resonator for slice-selective in vivo EPR imaging in rats. J Magn Reson 2008;190:124–134. [PubMed: 18006343]
34. Bueno, MDA.; Assis, AKT. Inductance and force calculations in electrical circuits. Nova Science Publishers, Inc; 2001.
35. Rochelle JM. Approximations for the symmetrical parallel-strip transmission line. IEEE Trans Microwave Theory Tech 1975;23:712–714.
36. Freed JH, Leniart DS, Hyde JS. Theory of saturation and double resonance effects in ESP spectra. RF coherence and line shapes. J Chem Phys 1967;47:2762–2773.
37. Pool, P. Electron Spin Resonance A Comprehensive Treatise on Experimental Techniques. Intersci. Publ. of John Wiley & Sons; New York, London, Sydney: 1983. p. 171-177.
38. Chzhan M, Shteynbuk M, Kuppusamy P, Zweier JL. An optimized L-band ceramic resonator for EPR imaging of biological samples. J Magn Reson 1993;A105:49–53.
39. Xia S, Villamena FA, Hadad CM, Kuppusamy P, Li Y, Zhu H, Zweier JL. Reactivity of Molecular oxygen with ethoxycarbonylderivatives of tetrathiatriarylmethyl radicals. J Org Chem 2006;71:7268–7279. [PubMed: 16958520]
40. Dhimitruka I, Velayutham M, Bobko AA, Khramtsov VV, Villamena F, Hadad CM, Zweier JL. Large scale synthesis of a trityl spin-probe for use in biomedical EPR imaging. Bioorg Med Chem Lett 2007;15;17(24):6801–6805.

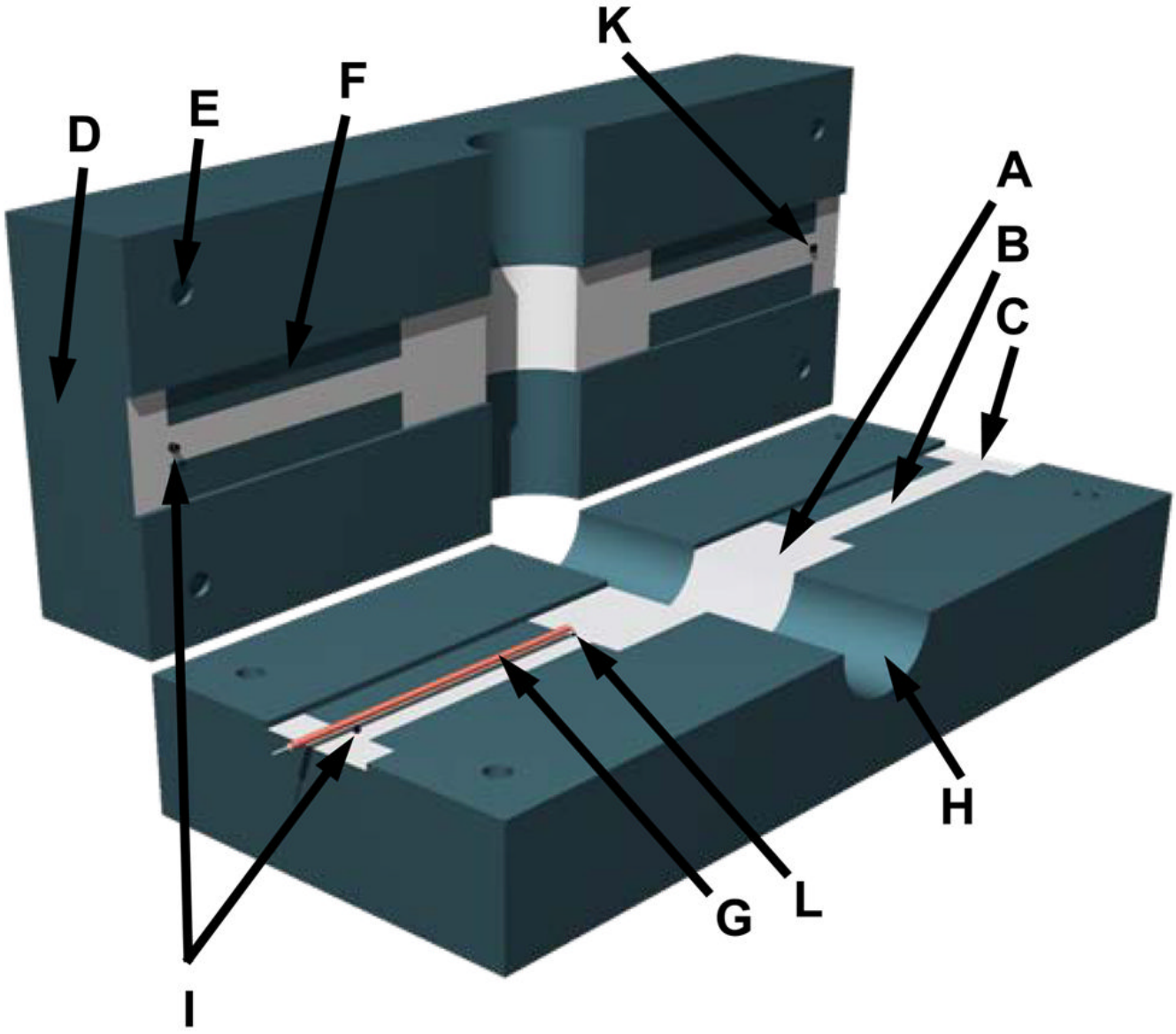

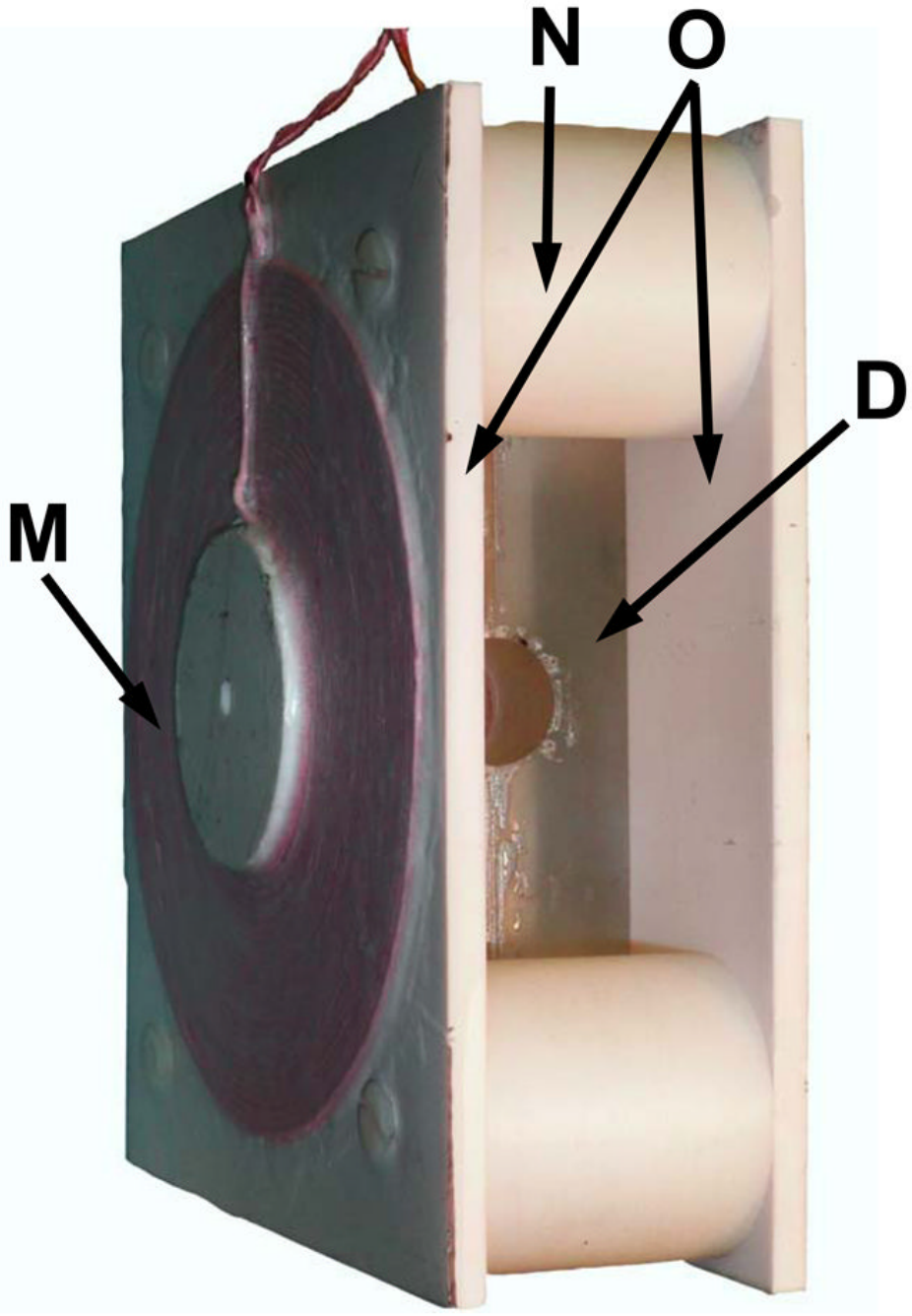

Figure 1.

(A) Layout of the dual mode EPR/NMR resonator (Resonator assembly). **A,** 19 mm wide capacitive element; **B,** 7 mm wide transmission line element; **C**, connection plates, **D**, resonator body; **E,** through hole; **F**, slot, 1.15 mm depth; **G,** coaxial cable, 1 mm diameter; **H,** 22 mm cylindrical bore for the sample; **I,** conductive short element (EPR side); **K**, 800 pF capacitor connection, and NMR feed connection (MRI side). **L.** 0.2 pF capacitor connection to coaxial cable (EPR side). (**B)** Photo of dual mode EPR/NMR resonator showing modulation coils assembly on either side of the resonator. **M,** modulation coil; **O,** spacers; **N,** modulation coil mounting plates; **D,** resonator body. Tuning and coupling variable capacitors are omitted from the drawings.

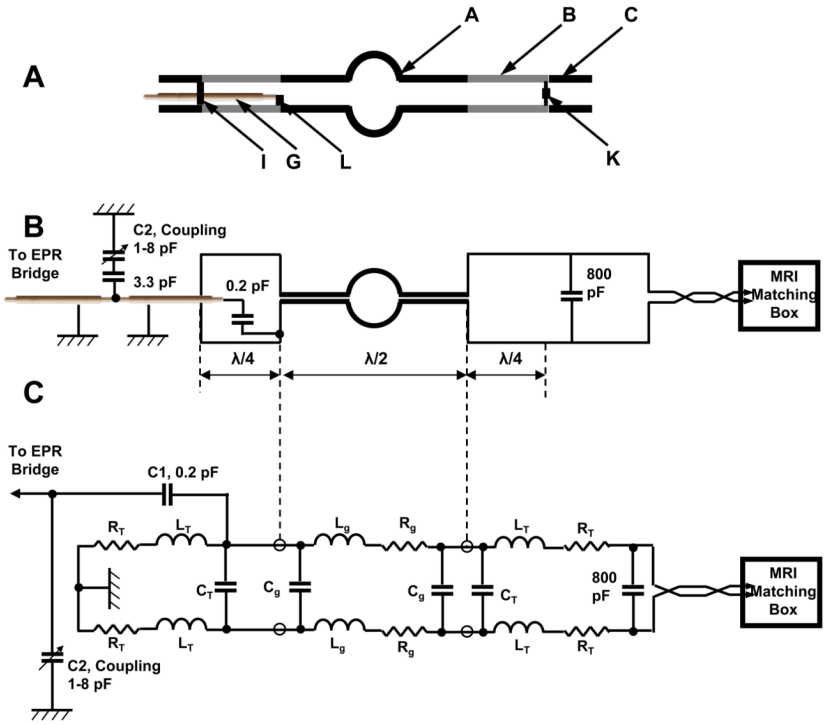

Figure 2.

(A) Line drawing of the conductive elements of the resonator. **A,** 19 mm wide capacitive element; **B,** transmission line element; **C**, connection plates, **G,** coaxial cable; **I,** conductive short element (EPR side); **K**, 800 pF capacitor connection, and NMR feed connection (MRI side). **L.** 0.2 pF capacitor connection to coaxial cable (EPR side). **(B)** Functional diagram of dual mode resonator assembly. (**C)** Equivalent circuit of the dual mode EPR/NMR resonator: $\mathbf{L_g}$,- inductance of the half 22 mm in diameter loop. **Cg**, capacitance of the 19 mm wide gap of the main resonator; $\mathbf{R_g}$ - resistance of the main loop conductor and loss inside the sample; $\mathbf{L_t}$ – equivalent distributional inductance of the 7 mm width transmission lines; $\mathbf{C_t}$ - equivalent distributional capacitance of the 7 mm width transmission lines; $\mathbf{R_T}$ - equivalent distributional resistance of the 7 mm wide transmission lines; C1 and C2 – equivalent capacitive divider of the coupling circuit.

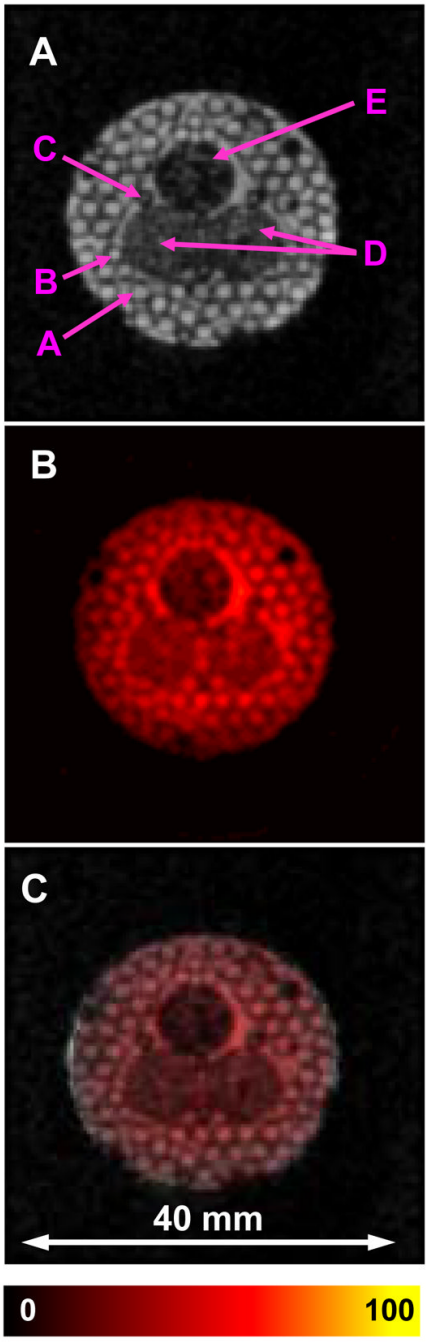

Figure 3.

A. Middle slice of 3D proton NMR image; **B.** Corresponding slice of 3D EPR image. **C.** Superposition of **A** and **B**. Phantom was constructed from tubes containing 1 mM TAM. The phantom consisted of 20 mm long clusters of capillary tubes of 1.3 mm ID (A), 0.9 mm ID (B), 0.5 mm ID (C), 2 tubes of 6 mm ID with TAM surrounding voids from packed 0.4 mm OD rods (D), 1 tube of 6 mm ID with TAM surrounding voids from packed 0.3 mm OD rods (E). The central 3 large tubes were arranged into a triangular shaped pattern, and all were packed into an 18 mm i.d. plastic cylinder. Images of this phantom demonstrate good sensitivity and accurate co-registration for EPR and NMR images. The parameters used for the EPRI acquisition: frequency 1.1 GHz, microwave power ~20 mW, modulation amplitude

0.03 mT at 100 kHz, field gradient 0.1 T/m, projection scan time 1.3 sec, 46×46 projections FOV 32×32 mm. 3D MRI images were collected using a conventional gradient echo pulse sequence with the imaging parameters: ^{1}H resonance frequency = 16.1805 MHz, spectral width = 10 kHz, TE/TR = 13/1000 ms, FOV = 32 mm, FOV in slice selection direction = 32 mm, Matrix size = 128 × 128 × 32, image orientation - axial, number of average = 1.

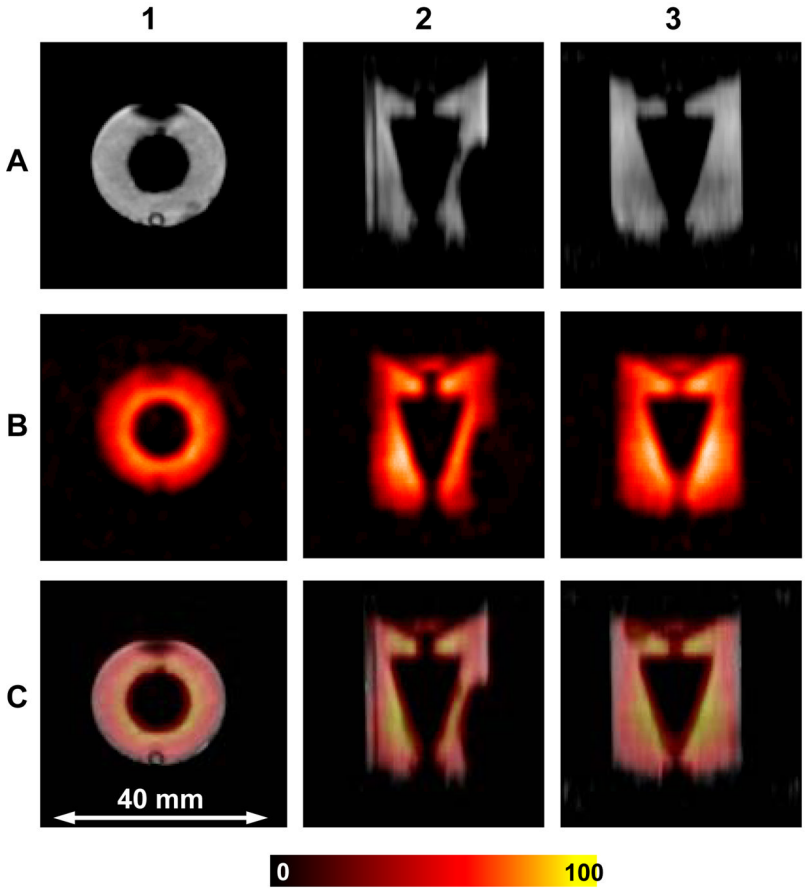

Figure 4.

Cylindrical phantom OD=19 mm with conical insert filled with 1 mM TAM. Row **A** shows MRI slices with axial (1), sagittal (2) and coronal (3) orientations. Row **B** shows the corresponding EPRI slices. Row C shows the superimposed images from **A** and **B** for each view. The parameters used for the EPRI acquisition: frequency 1.1 GHz, microwave power ~ 20 mW, modulation amplitude 0.03 mT at 100 kHz, field gradient 0.1 T/m, scan time 1.3 sec, FOV 32×32×32 mm 48×48 projections. The parameters for MRI: ^{1}H resonance frequency = 16.1805 MHz, spectral width = 10 kHz, excitation sinc pulse (pulse length = 2 ms, bandwidth = 3 kHz) flip angle = 90°, TE/TR = 13/1000 ms, FOV = 32 mm, FOV in slice selection direction = 32 mm, image orientation - axial, matrix size = 128 × 128 × 32, number of average = 1.

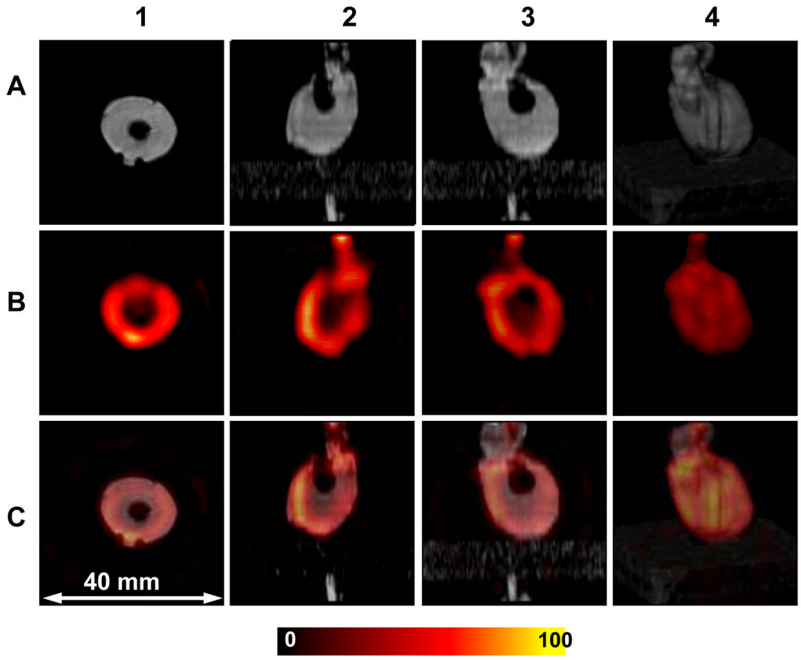

Figure 5.

Images of the isolated rat heart perfused with 1 mM TAM. Row **A** shows MRI slices with axial (1), sagittal (2) and coronal (3). Row **B** shows the corresponding axial, sagittal and coronal EPRI slices. Row **C** shows the superimposed images from **A** and **B** for each view. Additionally, on each row a 3-dimensional surface rendering of the MRI, EPRI signal matrix and the corresponding superimposed matrix are shown (4). The parameters used for the EPRI acquisition: frequency 1.1 GHz, microwave power ~20 mW, modulation amplitude 0.03 mT at 100 kHz, field gradient 0.1 T/m, scan time 1.3 sec, FOV 32×32×32 mm, 24×24 projections. The parameters for 3D gradient echo MRI: ^{1}H resonance frequency = 16.1805 MHz, spectral width = 10 kHz, excitation sinc pulse (pulse length = 2 ms, bandwidth = 3 kHz) flip angle = 90°, TE/TR = 13/1000 ms, FOV = 32 mm, FOV in slice selection direction = 32 mm, image orientation - axial, matrix size = 128 × 128 × 32, number of average = 1.

Table 1

EPR Microwave Parameters of the Dual Frequency Resonator and 25 mm Reentrant Resonator

Resonator	Empty resonators		Q Factor of the Resonators Loaded with 0.45 % saline solution		
	f_0 (GHz)	Q	1.5 cc	2.5 cc	4.5cc
Dual	1.175	195	144.3	90.3	60.4
Reentrant	1.083	301	196.0	89.7	59.1

J Magn Reson. Author manuscript; available in PMC 2011 July 1.